Nano Research 2017, 10(8): 2761–2771
DOI 10.1007/s12274-017-1480-z
Research Article
ISSN 1998-0124
CN 11-5974/O4

Transformation of monolayer MoS_2 into multiphasic $MoTe_2$: Chalcogen atom-exchange synthesis route

Qiyi Fang[1,2,§], Zhepeng Zhang[1,2,§], Qingqing Ji[2,§], Siya Zhu[1,3], Yue Gong[4,5,6], Yu Zhang[1,2], Jianping Shi[1,2], Xiebo Zhou[1,2], Lin Gu[4,5,6], Qian Wang[3,1], and Yanfeng Zhang[1,2] (✉)

[1] *Department of Materials Science and Engineering, College of Engineering, Peking University, Beijing 100871, China*
[2] *Center for Nanochemistry (CNC), Beijing National Laboratory for Molecular Sciences, College of Chemistry and Molecular Engineering, Academy for Advanced Interdisciplinary Studies, Peking University, Beijing 100871, China*
[3] *Center for Applied Physics and Technology, Peking University, Beijing 100871, China*
[4] *Beijing National Laboratory for Condensed Matter Physics, Institute of Physics, Chinese Academy of Sciences, Beijing 100190, China*
[5] *Collaborative Innovation Center of Quantum Matter, Beijing 100190, China*
[6] *School of Physical Sciences, University of Chinese Academy of Sciences, Beijing 100190, China*
[§] *These authors contributed equally to this work.*

Received: 12 October 2016
Revised: 11 January 2017
Accepted: 13 January 2017

KEYWORDS
transition-metal dichacogenide,
$MoTe_2$,
atom exchange,
multiphase,
phase transformation

ABSTRACT

Molybdenum ditelluride ($MoTe_2$), which is an important transition-metal dichalcogenide, has attracted considerable interest owing to its unique properties, such as its small bandgap and large Seebeck coefficient. However, the batch production of monolayer $MoTe_2$ has been rarely reported. In this study, we demonstrate the synthesis of large-domain (edge length exceeding 30 μm), monolayer $MoTe_2$ from chemical vapor deposition-grown monolayer MoS_2 using a chalcogen atom-exchange synthesis route. An in-depth investigation of the tellurization process reveals that the substitution of S atoms by Te is prevalently initiated at the edges and grain boundaries of the monolayer MoS_2, which differs from the homogeneous selenization of MoS_2 flakes with the formation of alloyed Mo–S–Se hybrids. Moreover, we detect a large compressive strain (approximately −10%) in the transformed $MoTe_2$ lattice, which possibly drives the phase transition from 2H to 1T′ at the reaction temperature of 500 °C. This phase change is substantiated by experimental facts and first-principles calculations. This work introduces a novel route for the templated synthesis of two-dimensional layered materials through atom substitutional chemistry and provides a new pathway for engineering the strain and thus the intriguing physics and chemistry.

Address correspondence to yanfengzhang@pku.edu.cn

1 Introduction

Semiconducting transition-metal dichalcogenides (TMD), such as MoS_2 and WS_2, have recently attracted considerable attention because of their intriguing properties, such as their direct bandgaps, strong light–matter interactions, and valley-related physics, which give them potential for a wide range of applications in electronics, optoelectronics [1, 2], catalysis [3, 4], etc. Compared with other group-VIB TMD layered materials, molybdenum ditelluride ($MoTe_2$) has intriguing features. Its bandgap of ~1.1 eV, which is comparable to that of silicon, together with its indirect-to-direct bandgap transition at the monolayer limit, makes this two-dimensional (2D) material a promising candidate for next-generation electronics and optoelectronics [5, 6].

Another distinct property of $MoTe_2$ compared with other TMDs is the small energy difference between its 2H and 1T′ phases (<0.1 eV per $MoTe_2$ unit) [7], which is beneficial for phase-memory applications and contact materials for field-effect transistors [8]. Additionally, 1T′-$MoTe_2$ was predicted to be a large-gap quantum spin Hall insulator [9] and thus may be suitable for a wide range of applications in novel switching devices [9] and spintronics [10, 11]. Recently, a topological Fermi arc was observed in the predicted type-II Weyl semimetal of $MoTe_2$, inspiring considerable research in this field [12, 13]. However, to realize such applications, the large-area, thickness-controllable synthesis of monolayer $MoTe_2$ is required. Recently, the direct synthesis of few-layer and even monolayer $MoTe_2$ has been realized by traditional chemical vapor deposition (CVD) [14–17]. Lee et al. fabricated centimeter-scale $MoTe_2$ thin films with a thickness of ~20 nm through the tellurization of Mo films [14] and tuned the phases of the $MoTe_2$ films by changing the tellurization time. Kong et al. synthesized few-layer $MoTe_2$ with different phases using disparate Mo precursors [15, 17]. Johnson et al. synthesized a 1T′-$MoTe_2$ monolayer with a novel star shape [16]. However, in these studies, the synthesized $MoTe_2$ was normally of the multilayer or 1T′ phase and had irregular shapes.

Post synthetic chemical transformations, such as ion-exchange reactions, have been regarded as facile and reliable methods for creating new materials and nanostructures, including II-VI, III-V, and VI-VI semiconductor compounds [18, 19], metal nanoparticles [20], and halide perovskites in liquid phases [21, 22]. Notably, a chalcogen atom-exchange reaction in the gas phase was utilized to achieve bandgap-tunable MoS_2Se_{2-x} alloys [23, 24].

Herein, we present the synthesis of monolayer $MoTe_2$ via a chalcogen atom-exchange synthesis route, i.e., by substituting the S atoms in monolayer MoS_2 with Te atoms. An MoS_2 monolayer template was synthesized on sapphire using low-pressure CVD (LPCVD), and the edge length of the triangular domain was as large as several tens of microns. Raman spectroscopy, atomic force microscopy (AFM), X-ray photoelectron spectroscopy (XPS), and transmission electron microscopy (TEM) were used to characterize the atom-exchange location and process, the chemical composition, and the crystal quality of the $MoTe_2$ samples obtained with different tellurization durations. Because of the different lattice constants of MoS_2 and $MoTe_2$, a compressive strain was observed in the tellurized region, and its effect on the phase transition of $MoTe_2$ (from 2H and 1T′ phases) was analyzed according to experimental data and theoretical calculations.

2 Results and discussion

MoS_2 monolayers with a lateral size up to tens of micrometers were synthesized by LPCVD, as previously reported [25, 26]. To synthesize multiphasic $MoTe_2$, the as-synthesized monolayer MoS_2/sapphire samples were placed downstream of a tube furnace, with Te powder upstream. H_2 and Ar were selected as carrier gases. The experimental setup is schematically shown in Fig. S1 (in the Electronic Supplementary Material (ESM)). By exposing the as-grown MoS_2 monolayers to Te vapor, S atoms were gradually substituted with Te atoms, according to the following reaction

$$MoS_2 + 2H_2 + 2Te \rightarrow MoTe_2 + 2H_2S \quad (1)$$

The substitution process is schematically shown in Fig. 1(a). The H_2 was necessary in the reaction process, as it prevented the oxidation of the MoS_2 samples by the minor residual oxygen. Figures 1(b) and 1(c) show optical images of an as-grown monolayer MoS_2

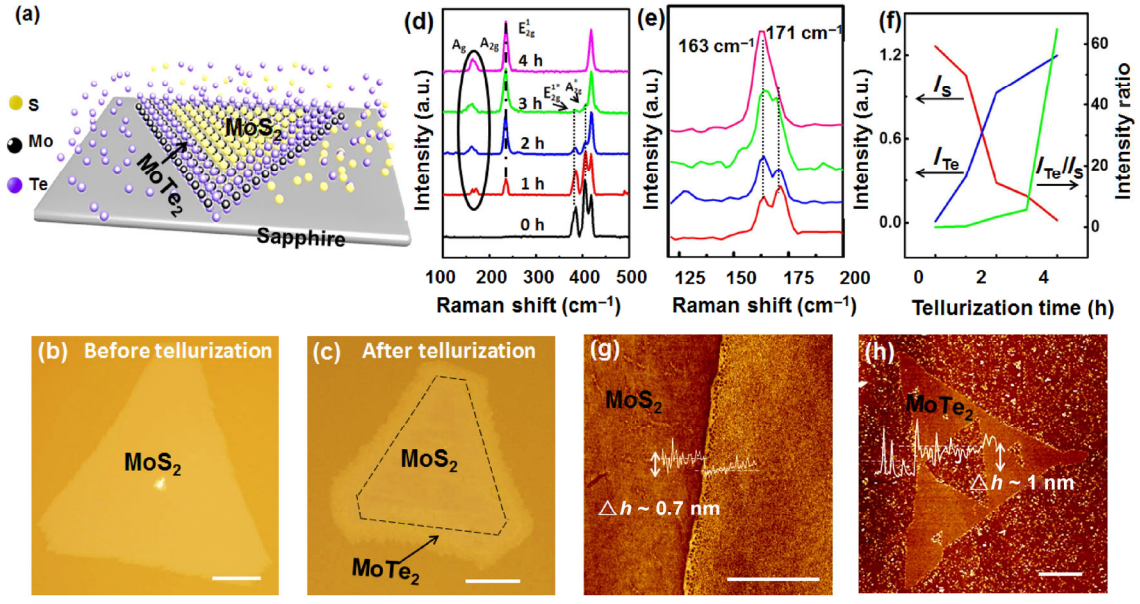

Figure 1 (a) Schematic of the chalcogen atom-exchange synthesis route for achieving monolayer $MoTe_2$ by using monolayer MoS_2 as a template. (b) and (c) Optical image of the as-synthesized MoS_2 and a sample tellurized for 1 h, exhibiting different contrasts between the peripheral and central regions distinguished by the dashed lines (scale bars represent 10 μm). (d) Average Raman spectra of a MoS_2 flake tellurized for 1, 2, 3, and 4 h. (e) Detailed Raman spectrum (120–200 cm^{-1}). (f) Evolution of the Raman peak intensity with respect to the tellurization time. (g) and (h) AFM images and corresponding height profiles showing the morphologies of monolayer MoS_2 and $MoTe_2$ (MoS_2 tellurized for 4 h), respectively.

triangular nanoflake and a nanoflake partially tellurized for 1 h, respectively. The size and the shape of the flake were almost unchanged after the tellurization, while slightly different contrasts are observed between the peripheral and central regions (indicated by the black dashed lines in Fig. 1(c)).

The chemical compositions of the MoS_2 samples after different tellurization durations (ranging from 0 to 4 h) were characterized by Raman spectroscopy. Figure 1(d) shows the averaged Raman spectra of the samples. Several Raman peaks in the range of 100–500 cm^{-1} are observed. The peak corresponding to the A_g mode of 1T′-$MoTe_2$ appeared at ~163 cm^{-1} [27]. The peaks corresponding to the out-of-plane A_{1g} mode and the in-plane E^1_{2g} mode of 2H-$MoTe_2$ [6] occurred at ~171 and ~234 cm^{-1}, respectively, and those corresponding to the in-plane E^{1*}_{2g} mode and the out-of-plane A^*_{1g} mode of 2H-MoS_2 [28, 29] occurred at ~387 and ~407 cm^{-1}, respectively. According to the tellurization time-dependent Raman spectra, the intensity of the $MoTe_2$-like Raman peaks increased significantly, and those of the MoS_2-like Raman peaks decreased after the tellurization, indicating that the nanoflakes were tellurized gradually with increasing reaction time. The final product was mainly composed of 2H-$MoTe_2$, along with a small portion of 1T′-$MoTe_2$. To further clarify the phase contribution, the Raman peaks at 171 and 163 cm^{-1} are emphasized in Fig. 1(e) for samples tellurized for different times. The Raman signals for 1T′-$MoTe_2$ and 2H-$MoTe_2$ are clearly observed, confirming the coexistence of the two phases.

The frequency difference between the E^{1*}_{2g} and A^*_{1g} modes of MoS_2 was ~20 cm^{-1}, and the out-of-plane B^1_{2g} mode was absent at ~289 cm^{-1}. These results indicate that the MoS_2 and tellurized samples had monolayer thickness [6, 30], which was confirmed by AFM and height-profile analyses (Figs. 1(g) and 1(h)). The original MoS_2 flake and the tellurized one exhibited heights of 0.7 and 1.0 nm, respectively, above the substrate. The normalized peak intensities of the E^1_{2g} mode of 2H-$MoTe_2$ and the A^*_{1g} mode of MoS_2, as well as their ratio, are plotted with respect to the tellurization time in Fig. 1(f). As the tellurization time increased, the peak intensity of the E^1_{2g} mode of 2H-$MoTe_2$ (I_{Te}) increased monotonically, whereas that of the A^*_{1g} mode of MoS_2 (I_S) decreased. This plot indicates the

substitution relationship between the two modes.

It is imperative to further understand the detailed tellurization dynamics of MoS_2, such as the initiation and propagation of $MoTe_2$ regions. Monolayer MoS_2 flakes with obvious defects and grain boundaries were tellurized for 1 h, as shown in the optical microscopy (OM) images of Figs. 2(a) and 2(e), respectively. Owing to the rapid decrease of the photoluminescence (PL) intensity of the tellurized samples (Fig. S2 in the ESM), Raman mapping was performed on these triangular and butterfly-like flakes, rather than PL mapping. Figures 2(b) and 2(f) show the spatial distributions of the Raman peak for 2H-MoS_2 at ~407 cm^{-1}. Figures 2(c) and 2(g) show the spatial distributions of the Raman peak for 2H-$MoTe_2$ at ~234 cm^{-1}. The Raman-mapping images clearly indicate that 2H-$MoTe_2$ was mainly distributed at the edges and defective sites (i.e., defects and grain boundaries) at the initial tellurization stage.

To provide additional details, Figs. 2(d) and 2(h) present the Raman spectra collected from three typical points at the edge, center region, and defective site (marked in Figs. 2(a) and 2(e), respectively). The typical Raman peaks for $MoTe_2$ and 2H-MoS_2 occurred at the edges and defective sites, whereas no Raman peaks of $MoTe_2$ occurred in the center regions. This possibly indicates that the tellurization initially occurred at the edges and defective sites, while the center region was relatively inert. Additionally, the peak intensity of 2H-$MoTe_2$ at the defective sites appeared to be far stronger than that at the edges, which agrees with previous reports indicating that the oxidation of TMDs initially occurs at the grain boundaries [31–33]. Thus, the S atoms at the defective sites were more preferably substituted with Te. To provide a clearer explanation, the possible tellurization channels are illustrated in Fig. 2(i). Considering the large size difference between the S and Te atoms, a significant lattice strain was expected in the tellurized regions. However, this compressive strain was more easily relaxed at the edges and defects (either grain boundaries or point defects) that had rich unsaturated coordination sites and thus abundant room for lattice relaxation (as schematically shown in Fig. S3 in the ESM). The unsaturated coordination characteristic of the edges and defective sites is a possible reason for the initial tellurization that preferentially occurred at the edges

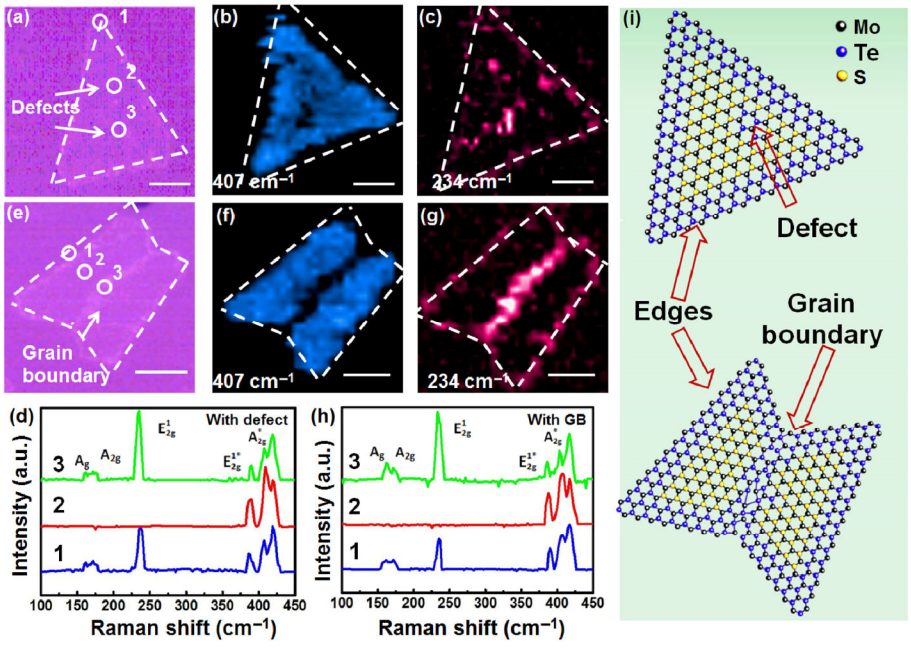

Figure 2 (a) and (e) Optical images of two typical MoS_2 nanoflakes characterized with defects and grain boundaries after tellurization for 1 h, respectively. (b) and (f) Raman mapping of the A_{2g}^{*} peak of MoS_2 (integrated from 380 to 420 cm^{-1}) and (c) and (g) the E_{2g}^{1} peak intensity of 2H-$MoTe_2$ (integrated from 210 to 250 cm^{-1}). (d) and (h) Raman spectra recorded for different sites (marked with circles labeled 1, 2, and 3) of the two samples (scale bars represent 10 μm). (i) Schematic of the tellurization, which initially occurred at the defects, edges, and grain boundaries.

and defective sites.

After continuous tellurization, additional S atoms were substituted with Te atoms. Figure 3(a) illustrates the model of continuous tellurization: The replacement of chalcogen atoms first occurred at the domain edges (neglect of defects) and gradually spread towards the center region, in a process similar to the diffusion of Te atoms from the edge to the center. To validate this, Figs. 3(b), 3(f), and 3(j) show OM images of the samples tellurized for 2, 3, and 4 h, respectively. The chemical compositions of the tellurized samples were determined by Raman mapping. Figures 3(c), 3(g), and 3(k) illustrate the intensity mapping of the Raman peak integrated from 380 to 420 cm^{-1}, and Figs. 3(d), 3(h), and 3(l) show the intensity mapping of the Raman peak integrated from 210 to 250 cm^{-1}. For 2 h tellurization, the peripheral regions were tellurized to $MoTe_2$, and the center regions remained nearly intact, as evidenced by the Raman mapping (Figs. 3(c) and 3(d)) and Raman spectra (Fig. 3(e)). Apparently, the typical peaks of MoS_2 occurred in the center region of the triangular flake, whereas the peak for $MoTe_2$ appeared at the periphery of the flake (Fig. 3(e)). After tellurization for 3 h, most of the S atoms were substituted with Te atoms. At the center of the triangular nanoflake, weak Raman peaks for MoS_2 were observed, as shown in Fig. 3(g). The S atoms were fully replaced by Te atoms after 4 h of tellurization. The detailed Raman spectra of three points from the edge to the center region are characterized by the signals from $MoTe_2$ (Figs. 3(e), 3(i), and 3(m)). When the tellurization time was increased from 2 to 4 h, the typical Raman peaks for $MoTe_2$ spread from the edge to the center regions of the samples, in parallel with

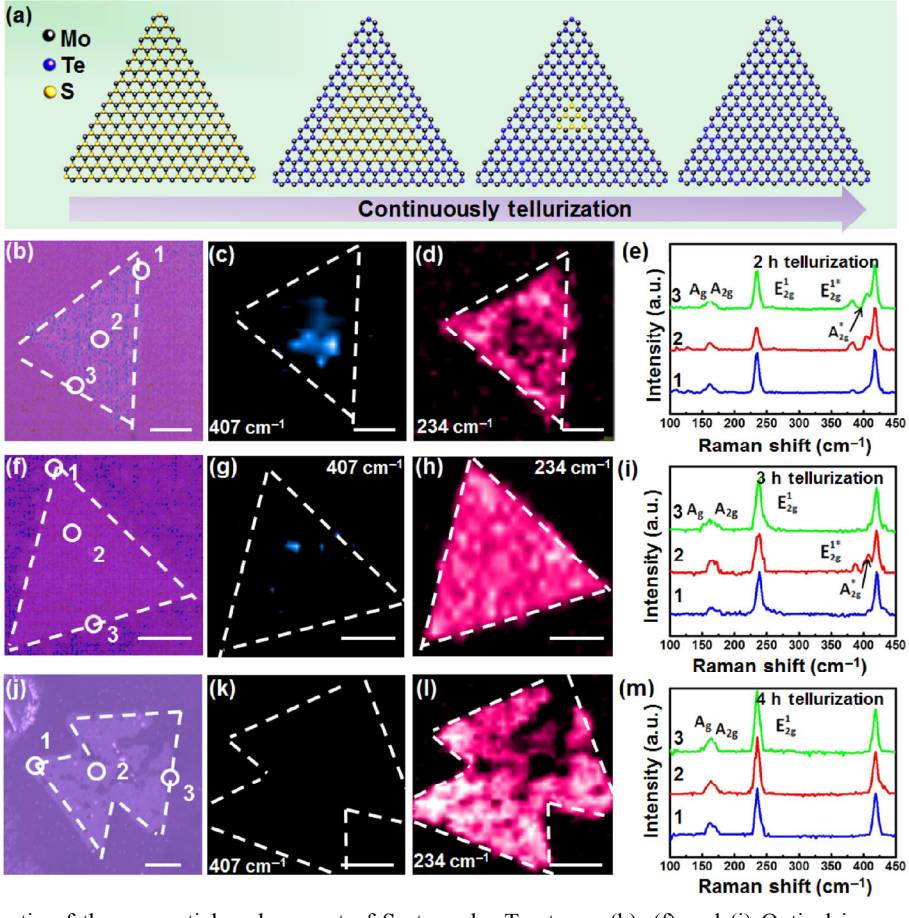

Figure 3 (a) Schematic of the sequential replacement of S atoms by Te atoms. (b), (f) and (j) Optical images of monolayer MoS_2 flakes tellurized for 2, 3, and 4 h, respectively. (c), (g), and (k) Raman maps of the A^*_{2g} peak of MoS_2 (integrated from 380 to 420 cm^{-1}) and (d), (h), and (l) the E^1_{2g} peak of 2H-$MoTe_2$ (integrated from 210 to 250 cm^{-1}). (e), (i), and (m) Raman spectra for different locations on the samples (scale bars represent 10 μm).

the full tellurization of MoS_2 at a specific timescale. The broken regions in Fig. 3(j) are attributed to the over-tellurization of the flake, which caused pits and holes via etching. As shown in Fig. S4 (in the ESM), AFM characterizations and height-profile analyses revealed cracks on the surface of the tellurized flakes due to the large lattice strain generated by the tellurization process.

According to theoretical calculations, the mixing energy of MoS_2 and $MoTe_2$ is more positive, and a high reaction temperature is needed for achieving their alloy phases [34, 35]. The critical temperature for complete miscibility was estimated to be 493 K [34], which is far lower than our tellurization temperature. This indicates that step-by-step tellurization occurred in our experiment, yielding pure $MoTe_2$ phases rather than alloys. This differs from the previously reported formation of compositional homogeneous alloys such as MoS_xSe_{2-x} and WS_xSe_{2-x} [23, 24, 36].

The tellurization process in this study is thus considered to have been controlled by the kinetic process, probably because of the large diameter difference between the Te and S atoms and the discrepancy between the lattice constants of MoS_2 (0.310 nm) and $MoTe_2$ (0.352 nm). Accordingly, the Te atoms did not easily replace the S atoms arranged in the perfect hexagonal lattice, considering that compressive strain occurred under homogenous tellurization on the nanoflake. Comparatively, the active S atoms at the edges and defective sites were more vulnerable to the tellurization because of their chemical reactivity; moreover, the strains at these sites were easily released through lattice reconstruction. The tellurization process is similar to the oxidation process that initially occurs at the edges and grain boundaries of monolayer TMDs [31–33]. Zheng et al. reported that the basal planes of 2H-phase MoS_2 can be activated for H evolution by increasing the number of single S vacancies [37]. A defect density as low as ~3% was predicted to reduce the energy of H adsorption from 2 to 0.2 eV in the H evolution reaction. Additionally, scanning tunneling microscopy/scanning tunneling spectroscopy (STM/STS) revealed that the bandgap at the domain edge was dramatically decreased from 2.20 to 0.3 eV for MoS_2/graphene/Au [38]. The high chemical activity and metallic characteristic of the defects and domain edges possibly promoted the tellurization via the chalcogen atom-exchange reaction.

XPS was performed to characterize the valence states and chemical-bonding structures of MoS_2 samples tellurized for different durations. Figure 4 shows the detailed scans for the S and Te binding energies for tellurization times of 1, 2, 3 and 4 h, with an untreated sample as a reference. The magnitude of each profile was normalized for visual comparison. Clearly, the as-grown MoS_2 sample exhibited two characteristic peaks at 162.1 and 163.3 eV, corresponding to the divalent S ions of the S $2p_{3/2}$ and S $2p_{1/2}$ orbitals [39]. After the tellurization, two doublet peaks appeared, which are assigned to Te and accord with the Mo–Te bonds at 572.9 eV (Te $3d_{5/2}$) and 583.2 eV (Te $3d_{3/2}$), matching previous XPS reports for this material [15]. Because of the unavoidable oxidation of the tellurized samples in the ambient conditions, a doublet peak assigned to the Te–O bonds at 576.5 eV (Te $3d^*_{5/2}$) and 586.9 eV (Te $3d^*_{3/2}$) was also observed [40]. Intriguingly, as the tellurization time increased, the XPS signals of S $2p_{3/2}$ and S $2p_{1/2}$ became less pronounced, whereas those of Te $3d_{5/2}$ and Te $3d_{3/2}$ became more prominent. After 4 h of tellurization, the doublet peak of S almost disappeared, and pure-Te peaks appeared, indicating the full conversion of S atoms into Te atoms and thus the phase transition from MoS_2 to $MoTe_2$. These results suggest that the tellurization time is a key parameter for chalcogen atomic-change synthesis.

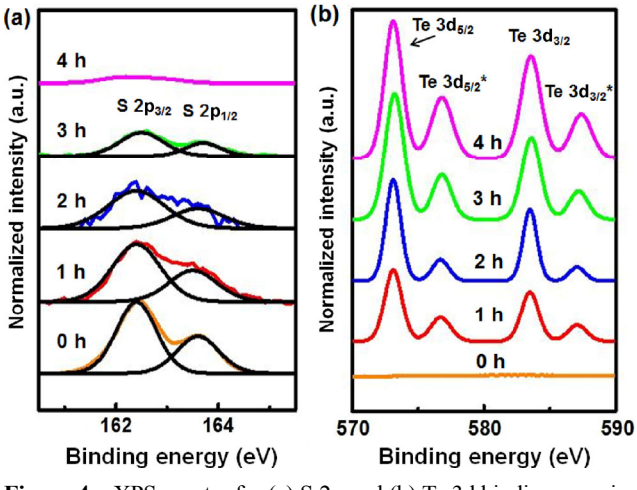

Figure 4 XPS spectra for (a) S 2p and (b) Te 3d binding energies for samples tellurized for different durations. The magnitude of each profile was normalized.

TEM was performed to clarify the structural difference between the MoS_2 template and the $MoTe_2$ product and thus confirm the formation of $MoTe_2$. Tellurized samples were transferred onto C films supported on Cu grids by a modified poly(methyl methacrylate)-assisted transfer method [40]. Figure 5(a) shows a large-scale TEM image of a hexagonal MoS_2 flake tellurized for 1 h. Here, different contrasts between the peripheral and center regions are observed, indicating a difference in the chemical composition between the two regions.

Selected-area electron diffraction (SAED) patterns were obtained for three typical regions: the center location (1), a peripheral location (3), and the interface (2) between the two. As shown in Figs. 5(b) and 5(d), only one set of sixfold-symmetric diffraction spots was observed, either on region 1 or region 3. The two sets of diffraction points exhibited the same lattice orientation but had different lattice vectors. At the interface (2), two sets of aligned diffraction points showing the same characteristic as those from locations (1) and (3) were observed, as shown in Fig. 5(c) (marked with green and red circles). To provide additional details, the intensity line profiles of the diffraction patterns along the dashed lines in Figs. 5(b)–5(d) were obtained, as shown in Fig. 5(e). The inverse lattice vectors of the two sets of diffraction points were thus estimated as 7.45 and 6.52 nm^{-1}, indicating lattice constants of 0.310 and 0.352 nm, respectively. Notably, the two lattice constants correspond well with those of 2H-MoS_2 and 2H-$MoTe_2$ [5], confirming the formation of monolayer $MoTe_2$. A high-resolution TEM (HRTEM) image of the interface is shown in Fig. 5(f). In the fast Fourier transform (FFT) image, the two sets

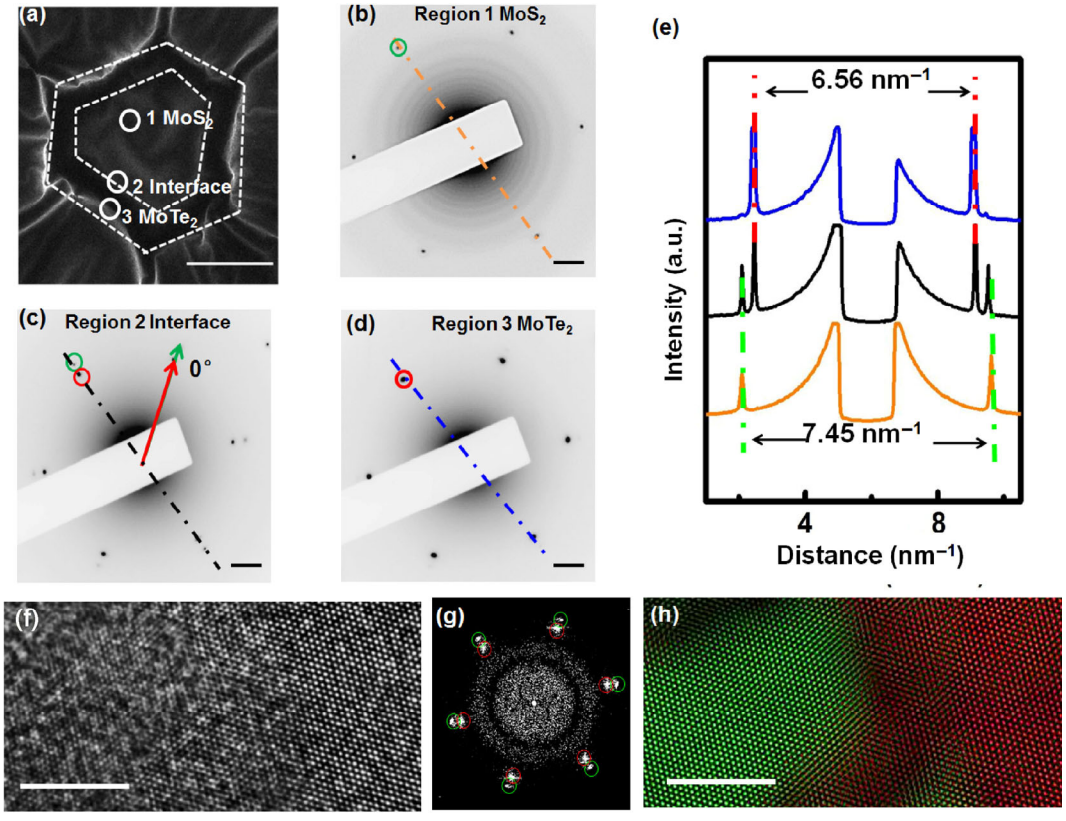

Figure 5 (a) Large-scale TEM image of monolayer MoS_2 after tellurization for 1 h (scale bars represent 10 μm). (b)–(d) SAED patterns for different locations on the TEM grid, labeled 1–3. Two sets of sixfold-symmetric diffraction points with the same orientation were observed in the interface location (scale bars represent 1 nm^{-1}). (e) Intensity line profiles of the SEAD patterns in (b)–(d). The two sets of diffraction patterns in (b) and (d) are attributed to MoS_2 and $MoTe_2$, respectively, whose parallel stacking is indicated by the interface locations in (c). (f) HRTEM image of a mildly tellurized sample containing both MoS_2 and $MoTe_2$. (g) FFT of the HRTEM image in (f). (h) IFFT of the HRTEM image. The MoS_2 and $MoTe_2$ signals are represented by green and red, respectively (scale bar: 5 nm).

of diffraction points corresponding to MoS_2 (green) and $MoTe_2$ (red) are the same as those shown in Fig. 5(c). To provide additional details, Fig. 5(h) shows the red and green inverse FFTs (IFFTs), indicating the composition distribution of the tellurized sample of Fig. 5(f). We infer that the $MoTe_2$ and MoS_2 regions were separated by a sharp interface. This TEM result agrees well with our previous prediction that the tellurization initially occurred at the edges of the nanoflakes and then gradually extended into the center region. Intriguingly, pure $MoTe_2$ layers evolved, rather than homogenous hybrids of Mo-S-Te, even at the intermediate tellurization stage.

Another interesting phenomenon is the formation of the 1T′ phase of $MoTe_2$. As previously reported, there was a small energy difference between the 1T′ and 2H phases of $MoTe_2$, and the latter phase was more preferable for the synthesis [15, 41]. However, in our case, the Raman peak of 1T′-$MoTe_2$ was also noticeable in the tellurized regions (Figs. 1(d) and 1(e)). Thus, an exotic factor may have affected the phase diagram. Figures 6(a) and 6(b) show the energies of the strained and unstrained monolayer $MoTe_2$ in the three typical phases of 1T, 1T′, and 2H, which were calculated using first-principles density functional theory (DFT) [42]. In the unstrained state (Fig. 6(a)), the minimum energy of 2H-$MoTe_2$ in the temperature range of 0 to 1,000 K was constantly lower than that of the 1T′ phase, implying that the 2H phase was more energetically preferable in this temperature range. This agrees well with previous calculations.

However, in our case, considering the substitution chemistry of the MoS_2 templates, if the lattice constant remained intact during the tellurization, the compressive strain in the hexagonal lattice of the resulting $MoTe_2$ was as large as −10%, as estimated by $(a_{MoS_2} - a_{MoTe_2})/a_{MoTe_2}$. For simplicity, the lattice constants of the 1T′ and 1T phases in the equilibrium states were considered to be the same as that of the H-phase, which did not influence the qualitative results. Thus, for ε = −10%, the Helmholtz free energy of the 2H phase (calculated from 0 to 1,000 K) was higher than that of the 1T′ phase above 630 K (Fig. 6(b)). This may explain why the phase transformation from 2H to 1T′ occurred at a high temperature under the strained condition. This type of phase transition was observed in a previous study [43], where the homogeneous and reversible semiconductor-metal phase transition of $MoTe_2$ was observed at a tensile strain of 0.2% at room temperature.

To provide additional details, the Helmholtz free energies of different phases with and without strain at a high temperature (~770 K) are plotted in Fig. 6(c). This temperature is very close to the tellurization temperature used in our experiment. Obviously, in the strained state, the 1T′ phase is more stable than

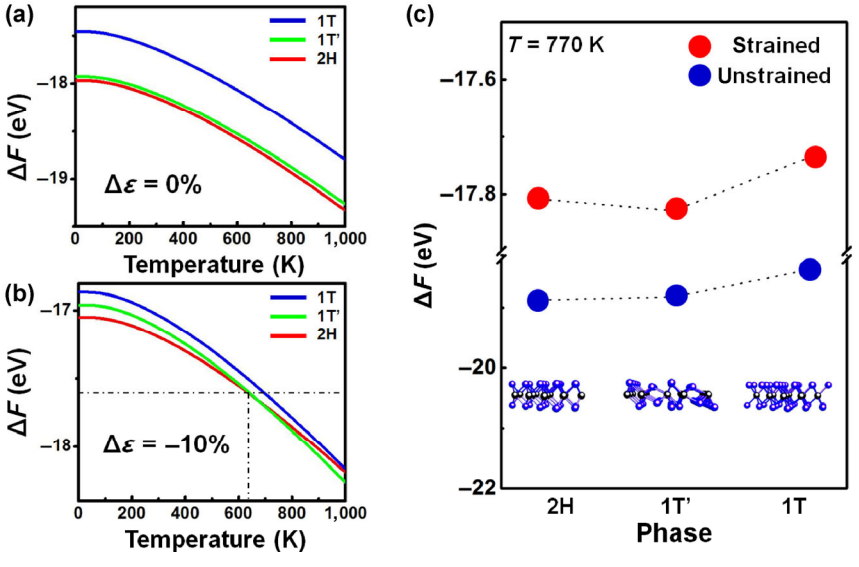

Figure 6 Theoretical calculation of the formation energies of the different phases (1T, 1T', and 2H) of (a) unstrained and (b) strained monolayer $MoTe_2$. (c) Formation energies of different phases of monolayer $MoTe_2$ with and without strain under 770 K.

the 2H phase during such a high-temperature growth process. However, when the sample was cooled to room temperature, the 1T′-$MoTe_2$ was transformed into the 2H phase, as indicated by the crossover of the ground state from 1T′ to 2H below 630 K. This tentative theoretical calculation indicates that the 1T′ and 2H phases coexisted in the tellurized regions, as confirmed by our experimental data.

3 Conclusions

Multiphasic mixed $MoTe_2$ monolayers were synthesized using a novel chalcogen atom-exchange route. The replacement of the chalcogen atoms preferably occurred at the defective sites and the edges of the nanoflakes. Intriguingly, compared with the case of the Mo-S-Se system, the replacement for the Mo-S-Te system was inhomogeneous on the flakes, and the formation of nearly pure $MoTe_2$ was more favorable even at the intermediate tellurization stage. Because of the large lattice mismatch of MoS_2 and $MoTe_2$, a large compressive strain was observed in the tellurized nanoflakes, possibly driving the phase transformation from 2H to 1T′. This work presents a feasible route for the synthesis of monolayer $MoTe_2$ and provides an in-depth understanding of the phase transformation in 2D TMD layers.

4 Experimental

4.1 Synthesis of monolayer MoS_2 on sapphire

The MoS_2 samples were grown inside a multi-temperature zone tubular furnace (Lindberg/Blue M) equipped with a 1-in-diameter quartz tube. S powder was placed outside the hot zone and mildly sublimated with heating belts at ~115 ℃. MoO_3 powder (Alfa Aesar, purity 99.9%) and as-received sapphire (0001) substrates with no pretreatments were successively placed in the hot center of the tube furnace. The tube was pumped down to a base pressure of ~1 Pa and repeatedly flushed with Ar carrier gas to guarantee a favorable growth atmosphere. To achieve large-domain size MoS_2 flakes, air was introduced into the growth chamber [25]. The flow rate of the Ar was ~100 sccm. The flow rate of air was controlled according to the total pressure in the chamber. The growth conditions were optimized at a pressure of ~35 Pa, a MoO_3 sublimation temperature of ~530 ℃, a growth temperature of ~850 ℃, and a growth time of 20 min.

4.2 Tellurization of MoS_2

The as-grown MoS_2 samples were placed in the center of a multi-temperature zone tubular furnace (Lindberg/Blue M) equipped with a 1-in-diameter quartz tube. Te powders were placed at the upstream position next to the MoS_2 samples. The furnace was heated to 500 ℃ in 30 min with 10-sccm Ar and 4-sccm H_2 and maintained for different durations (1–4 h).

4.3 Characterization

The monolayer MoS_2 and tellurized samples were systematically characterized using OM (Nikon LV100ND), XPS (Kratos AXIS Supra/Ultra with monochromatic Al Kα X-ray), AFM (Dimension Icon, Bruker), scanning electron microscopy (Hitachi S-4800; acceleration voltage of 1–5 kV), and TEM (FEI, Tecnai F20; acceleration voltage of 200 kV).

4.4 DFT calculation

DFT calculations were performed using the Vienna *ab-initio* simulation package [44] at the level of the generalized gradient approximation with the Perdew–Burke–Ernzerhof (PBE) [45] exchange and the correlation functional. The cutoff energy of the plane-wave basis set was 400 eV. The thermal properties were calculated using the finite-displacement method in the program Phonopy [46], and supercells of 5 × 5 × 1 were employed. For the DFT and thermal-property calculations of H-phase, T-phase, and T′-phase $MoTe_2$ nanosheets, a vacuum space of 15 Å was used to avoid interactions between the layers.

Acknowledgements

We acknowledge financial support by National Natural Science Foundation of China (Nos. 51472008, 51290272, 51471004, and 51672307), the National High-tech R&D Program of China (No. 2016YFA0200103), the National Basic Research Program of China (No. 2014CB921002), the Open Research Fund Program of the State Key

Laboratory of Low-Dimensional Quantum Physics (No. KF201601), the Strategic Priority Research Program of Chinese Academy of Sciences (No. XDB07030200) and the Key Research Program of Frontier Sciences, CAS (No. QYZDB-SSW-JSC035).

Electronic Supplementary Material: Supplementary material (experimental setup, photoluminescence measurements, schematic of the in plane strains and relaxation path ways of tellurized samples and AFM image) is available in the online version of this article at https://doi.org/10.1007/s12274-017-1480-z.

References

[1] Radisavljevic, B.; Radenovic, A.; Brivio, J.; Giacometti, V.; Kis, A. Single-layer MoS_2 transistors. *Nat. Nanotechnol.* **2011**, *6*, 147–150.

[2] Wang, Q. H.; Kalantar-Zadeh, K.; Kis, A.; Coleman, J. N.; Strano, M. S. Electronics and optoelectronics of two-dimensional transition metal dichalcogenides. *Nat. Nanotechnol.* **2012**, *7*, 699–712.

[3] Kibsgaard, J.; Chen, Z. B.; Reinecke, B. N.; Jaramillo, T. F. Engineering the surface structure of MoS_2 to preferentially expose active edge sites for electrocatalysis. *Nat. Mater.* **2012**, *11*, 963–969.

[4] Shi, J. P.; Ma, D. L.; Han, G.-F.; Zhang, Y.; Ji, Q. Q.; Gao, T.; Sun, J. Y.; Song, X. J.; Li, C.; Zhang, Y. S. et al. Controllable growth and transfer of monolayer MoS_2 on Au foils and its potential application in hydrogen evolution reaction. *ACS Nano* **2014**, *8*, 10196–10204.

[5] Balendhran, S.; Walia, S.; Nili, H.; Ou, J. Z.; Zhuiykov, S.; Kaner, R. B.; Sriram, S.; Bhaskaran, M.; Kalantar-Zadeh, K. Two-dimensional molybdenum trioxide and dichalcogenides. *Adv. Funct. Mater.* **2013**, *23*, 3952–3970.

[6] Ruppert, C.; Aslan, O. B.; Heinz, T. F. Optical properties and band gap of single- and few-layer $MoTe_2$ crystals. *Nano Lett.* **2014**, *14*, 6231–6236.

[7] Duerloo, K.-A. N.; Li, Y.; Reed, E. J. Structural phase transitions in two-dimensional Mo- and W-dichalcogenide monolayers. *Nat. Commun.* **2014**, *5*, 4214.

[8] Cho, S.; Kim, S.; Kim, J. H.; Zhao, J.; Seok, J.; Keum, D. H.; Baik, J.; Choe, D.-H.; Chang, K. J.; Suenaga, K. et al. Phase patterning for ohmic homojunction contact in $MoTe_2$. *Science* **2015**, *349*, 625–628.

[9] Qian, X. F.; Liu, J. W.; Fu, L.; Li, J. Quantum spin Hall effect in two-dimensional transition metal dichalcogenides. *Science* **2014**, *346*, 1344–1347.

[10] Gong, Z. R.; Liu, G.-B.; Yu, H. Y.; Xiao, D.; Cui, X. D.; Xu, X. D.; Yao, W. Magnetoelectric effects and valley-controlled spin quantum gates in transition metal dichalcogenide bilayers. *Nat. Commun.* **2013**, *4*, 2053.

[11] Kane, C. L.; Mele, E. J. Quantum spin hall effect in graphene. *Phys. Rev. Lett.* **2005**, *95*, 226801.

[12] Huang, L.; McCormick, T. M.; Ochi, M.; Zhao, Z. Y.; Suzuki, M.-T.; Arita, R.; Wu, Y.; Mou, D. X.; Cao, H. B.; Yan, J. Q. et al. Spectroscopic evidence for a type II Weyl semimetallic state in $MoTe_2$. *Nat. Mater.* **2016**, *15*, 1155–1160.

[13] Deng, K.; Wan, G. L.; Deng, P.; Zhang, K. N.; Ding, S. J.; Wang, E. Y.; Yan, M. Z.; Huang, H. Q.; Zhang, H. Y.; Xu, Z. L. et al. Experimental observation of topological Fermi arcs in type-II Weyl semimetal $MoTe_2$. *Nat. Phys.* **2016**, *12*, 1105–1110.

[14] Park, J. C.; Yun, S. J.; Kim, H.; Park, J.-H.; Chae, S. H.; An, S.-J.; Kim, J.-G.; Kim, S. M.; Kim, K. K.; Lee, Y. H. Phase-engineered synthesis of centimeter-scale 1T′- and 2H-molybdenum ditelluride thin films. *ACS Nano* **2015**, *9*, 6548–6554.

[15] Zhou, L.; Xu, K.; Zubair, A.; Liao, A. D.; Fang, W. J.; Ouyang, F. P.; Lee, Y.-H.; Ueno, K.; Saito, R.; Palacios, T. et al. Large-area synthesis of high-quality uniform few-layer $MoTe_2$. *J. Am. Chem. Soc.* **2015**, *137*, 11892–11895.

[16] Naylor, C. H.; Parkin, W. M.; Ping, J. L.; Gao, Z. L.; Zhou, Y. R.; Kim, Y.; Streller, F.; Carpick, R. W.; Rappe, A. M.; Drndić, M. et al. Monolayer single-crystal 1T′-$MoTe_2$ grown by chemical vapor deposition exhibits weak antilocalization effect. *Nano Lett.* **2016**, *16*, 4297–4304.

[17] Zhou, L.; Zubair, A.; Wang, Z. Q.; Zhang, X.; Ouyang, F. P.; Xu, K.; Fang, W. J.; Ueno, K.; Li, J.; Palacios, T. et al. Synthesis of high-quality large-area homogenous 1T' $MoTe_2$ from chemical vapor deposition. *Adv. Mater.* **2016**, *28*, 9526–9531.

[18] Jain, P. K.; Amirav, L.; Aloni, S.; Alivisatos, A. P. Nanoheterostructure cation exchange: Anionic framework conservation. *J. Am. Chem. Soc.* **2010**, *132*, 9997–9999.

[19] Li, H. B.; Zanella, M.; Genovese, A.; Povia, M.; Falqui, A.; Giannini, C.; Manna, L. Sequential cation exchange in nanocrystals: Preservation of crystal phase and formation of metastable phases. *Nano Lett.* **2011**, *11*, 4964–4970.

[20] Son, D. H.; Hughes, S. M.; Yin, Y. D.; Paul Alivisatos, A. Cation exchange reactions in ionic nanocrystals. *Science* **2004**, *306*, 1009–1012.

[21] Wong, A. B.; Lai, M. L.; Eaton, S. W.; Yu, Y.; Lin, E.; Dou, L. T.; Fu, A.; Yang, P. D. Growth and anion exchange conversion of $CH_3NH_3PbX_3$ nanorod arrays for light-emitting diodes. *Nano Lett.* **2015**, *15*, 5519–5524.

[22] Zhang, D. D.; Yang, Y. M.; Bekenstein, Y.; Yu, Y.; Gibson, N. A.; Wong, A. B.; Eaton, S. W.; Kornienko, N.; Kong, Q.; Lai, M. L. et al. Synthesis of composition tunable and highly luminescent cesium lead halide nanowires through anion-exchange reactions. *J. Am. Chem. Soc.* **2016**, *138*, 7236–7239.

[23] Ma, Q.; Isarraraz, M.; Wang, C. S.; Preciado, E.; Klee, V.; Bobek, S.; Yamaguchi, K.; Li, E.; Odenthal, P. M.; Nguyen, A. et al. Postgrowth tuning of the bandgap of single-layer molybdenum disulfide films by sulfur/selenium exchange. *ACS Nano* **2014**, *8*, 4672–4677.

[24] Su, S.-H.; Hsu, Y.-T.; Chang, Y.-H.; Chiu, M.-H.; Hsu, C.-L.; Hsu, W.-T.; Chang, W.-H.; He, J.-H.; Li, L.-J. Band gap-tunable molybdenum sulfide selenide monolayer alloy. *Small* **2014**, *10*, 2589–2594.

[25] Chen, W.; Zhao, J.; Zhang, J.; Gu, L.; Yang, Z. Z.; Li, X. M.; Yu, H.; Zhu, X. T.; Yang, R.; Shi, D. X. et al. Oxygen-assisted chemical vapor deposition growth of large single-crystal and high-quality monolayer MoS_2. *J. Am. Chem. Soc.* **2015**, *137*, 15632–15635.

[26] Ji, Q. Q.; Kan, M.; Zhang, Y.; Guo, Y.; Ma, D. L.; Shi, J. P.; Sun, Q.; Chen, Q.; Zhang, Y. F.; Liu, Z. F. Unravelling orientation distribution and merging behavior of monolayer MoS_2 domains on sapphire. *Nano Lett.* **2015**, *15*, 198–205.

[27] Keum, D. H.; Cho, S.; Kim, J. H.; Choe, D.-H.; Sung, H.-J.; Kan, M.; Kang, H.; Hwang, J.-Y.; Kim, S. W.; Yang, H. et al. Bandgap opening in few-layered monoclinic $MoTe_2$. *Nat. Phys.* **2015**, *11*, 482–486.

[28] Lee, C.; Yan, H. G.; Brus, L. E.; Heinz, T. F.; Hone, J.; Ryu, S. Anomalous lattice vibrations of single- and few-layer MoS_2. *ACS Nano* **2010**, *4*, 2695–2700.

[29] Li, H.; Zhang, Q.; Yap, C. C. R.; Tay, B. K.; Edwin, T. H. T.; Olivier, A.; Baillargeat, D. From bulk to monolayer MoS_2: Evolution of Raman scattering. *Adv. Funct. Mater.* **2012**, *22*, 1385–1390.

[30] Molina-Sánchez, A.; Wirtz, L. Phonons in single-layer and few-layer MoS_2 and WS_2. *Phys. Rev. B* **2011**, *84*, 155413.

[31] Rong, Y. M.; He, K.; Pacios, M.; Robertson, A. W.; Bhaskaran, H.; Warner, J. H. Controlled preferential oxidation of grain boundaries in monolayer tungsten disulfide for direct optical imaging. *ACS Nano* **2015**, *9*, 3695–3703.

[32] Zhang, Y.; Zhang, Y. F.; Ji, Q. Q.; Ju, J.; Yuan, H. T.; Shi, J. P.; Gao, T.; Ma, D. L.; Liu, M. X.; Chen, Y. B. et al. Controlled growth of high-quality monolayer WS_2 layers on sapphire and imaging its grain boundary. *ACS Nano* **2013**, *7*, 8963–8971.

[33] Liu, Y. N.; Tan, C.; Chou, H.; Nayak, A.; Wu, D.; Ghosh, R.; Chang, H.-Y.; Hao, Y. F.; Wang, X. H.; Kim, J.-S. et al. Thermal oxidation of WSe_2 nanosheets adhered on SiO_2/Si substrates. *Nano Lett.* **2015**, *15*, 4979–4984.

[34] Kang, J.; Tongay, S.; Li, J. B.; Wu, J. Q. Monolayer semiconducting transition metal dichalcogenide alloys: Stability and band bowing. *J. Appl. Phys.* **2013**, *113*, 143703.

[35] Komsa, H.-P.; Krasheninnikov, A. V. Two-dimensional transition metal dichalcogenide alloys: Stability and electronic properties. *J. Phys. Chem. Lett.* **2012**, *3*, 3652–3656.

[36] Li, H. L.; Duan, X. D.; Wu, X. P.; Zhuang, X. J.; Zhou, H.; Zhang, Q. L.; Zhu, X. L.; Hu, W.; Ren, P. Y.; Guo, P. F. et al. Growth of alloy $MoS_{2x}Se_{2(1-x)}$ nanosheets with fully tunable chemical compositions and optical properties. *J. Am. Chem. Soc.* **2014**, *136*, 3756–3759.

[37] Li, H.; Tsai, C.; Koh, A. L.; Cai, L. L.; Contryman, A. W.; Fragapane, A. H.; Zhao, J. H.; Han, H. S.; Manoharan, H. C.; Abild-Pedersen, F. et al. Activating and optimizing MoS_2 basal planes for hydrogen evolution through the formation of strained sulphur vacancies. *Nat. Mater.* **2016**, *15*, 48–53.

[38] Shi, J. P.; Zhou, X. B.; Han, G.-F.; Liu, M. X.; Ma, D. L.; Sun, J. Y.; Li, C.; Ji, Q. Q.; Zhang, Y.; Song, X. J. et al. Narrow-gap quantum wires arising from the edges of monolayer MoS_2 synthesized on graphene. *Adv. Mater. Interfaces* **2016**, *3*, 1600332.

[39] Wang, X. S.; Feng, H. B.; Wu, Y. M.; Jiao, L. Y. Controlled synthesis of highly crystalline MoS_2 flakes by chemical vapor deposition. *J. Am. Chem. Soc.* **2013**, *135*, 5304–5307.

[40] Ma, D. L.; Shi, J. P.; Ji, Q. Q.; Chen, K.; Yin, J. B.; Lin, J. B.; Zhang, Y.; Liu, M. X.; Feng, Q. L.; Song, X. J. et al. A universal etching-free transfer of MoS_2 films for applications in photodetectors. *Nano Res.* **2015**, *8*, 3662–3672.

[41] Sun, Y. F.; Wang, Y. X.; Sun, D.; Carvalho, B. R.; Read, C. G.; Lee, C.-H.; Lin, Z.; Fujisawa, K.; Robinson, J. A.; Crespi, V. H. et al. Low-temperature solution synthesis of few-layer 1T ′-$MoTe_2$ nanostructures exhibiting lattice compression. *Angew. Chem., Int. Ed.* **2016**, *55*, 2830–2834.

[42] Kan, M.; Wang, B.; Lee, Y. H.; Sun, Q. A density functional theory study of the tunable structure, magnetism and metal-insulator phase transition in VS_2 monolayers induced by in-plane biaxial strain. *Nano Res.* **2015**, *8*, 1348–1356.

[43] Song, S.; Keum, D. H.; Cho, S.; Perello, D.; Kim, Y.; Lee, Y. H. Room temperature semiconductor–metal transition of $MoTe_2$ thin films engineered by strain. *Nano Lett.* **2016**, *16*, 188–193.

[44] Kresse, G.; Furthmüller, J. Efficient iterative schemes for *ab initio* total-energy calculations using a plane-wave basis set. *Phys. Rev. B* **1996**, *54*, 11169–11186.

[45] Perdew, J. P.; Burke, K.; Ernzerhof, M. Generalized gradient approximation made simple. *Phys. Rev. Lett.* **1996**, *77*, 3865–3868.

[46] Togo, A.; Tanaka, I. First principles phonon calculations in materials science. *Scr. Mater.* **2015**, *108*, 1–5.